



ELSEVIER

Contents lists available at ScienceDirect

Radiation Physics and Chemistry

journal homepage: www.elsevier.com/locate/radphyschem

Characterization of prototype perforated semiconductor neutron detectors

C.M. Henderson, Q.M. Jahan, W.L. Dunn*, J.K. Shultis, D.S. McGregor

Department of Mechanical and Nuclear Engineering, Kansas State University, 3002 Rathbone Hall, Manhattan, KS 66506, USA

ARTICLE INFO

Article history:

Received 13 May 2009

Accepted 30 July 2009

Keywords:

Dosimeter

Neutron

Semiconductor

Dose

Imaging

ABSTRACT

Semiconductor detectors whose surfaces are coated with neutron-reactive material can be made to detect thermal neutrons, but with efficiencies only of a few percent. However, perforating the semiconductor material, filling the perforations with neutron-reactive material, and then coating the detector surface can lead to neutron detectors of much higher thermal neutron detection efficiencies, perhaps approaching or exceeding 50%. Several perforated semiconductor neutron detectors have been constructed, both for dosimetry and for position-sensitive neutron detection. The characterization of prototype devices based on these detectors is described.

© 2009 Elsevier Ltd. All rights reserved.

1. Introduction

Neutrons generally are detected by measuring directly ionizing radiation that is generated as a result of neutron interactions with nuclei in the detector. Detectors based on this principle include gas-filled, scintillation, and semiconductor detectors (Knoll, 2000). Gas-filled neutron detectors include BF_3 and ^3He proportional counters, fission chambers, and boron- or gadolinium-lined tubes. Scintillation neutron detectors include B_2O_3 fused with ZnS (which has found use in neutron time-of-flight studies), boronated plastic scintillators (in bulk or as fibers), and lithium iodide crystals activated by a small amount of Eu (Nicholson and Snelling, 1955). Semiconductor detectors coated with a neutron-reactive material, such as ^{10}B or ^6LiF , are capable of neutron detection, but only at thermal detection efficiencies below 5% for singly coated devices and below 10% for doubly coated devices (McGregor et al., 2003).

Active neutron dosimeters based on gas-filled detectors include tissue-equivalent proportional counters (Badhwar, 2002) and Bonner spheres (Esposito and Nandy, 2004), both of which are useful for area dosimetry but are too bulky to be worn as personal dosimeters. Coated semiconductor detectors can in principle be used as neutron dosimeters but their low detection efficiency limits their neutron sensitivity. Passive neutron dosimeters, in which neutrons induce some change in the dosimeter that is measured at a later time, include bubble dosimeters (Riel et al., 1991), etch-track dosimeters (Ing and Piesch, 1985), and thermoluminescent dosimeters (TLDs) (Aschan et al., 1999). However,

bubble dosimeters have problems with reliability and durability (ICRU, 2001), the performance of etch-track dosimeters varies from batch to batch and is affected by aging of the plastic, and TLDs in the form of albedo neutron dosimeters (Piesch and Burgkhardt, 1985) are dependent on neutron energy, are photon sensitive, and do not measure low doses well (ICRU, 2001).

Arrays of neutron detectors are useful for neutron scattering and imaging studies. Intense neutron sources—such as the ISIS pulsed source in the UK, the Opal reactor in Australia, and the Spallation Neutron Source (SNS) in the US—offer unique opportunities for materials analysis research using neutrons. In order to take advantage of the opportunities offered by these high-intensity sources, high-resolution (sub-mm) neutron detector arrays are needed. Arrays of gas and scintillation detectors can achieve good angular resolution, but only by placing the arrays far from the sample. Semiconductor arrays, which can achieve good spatial resolution and thus can be placed near the sample, offer the advantage that neutron interactions in the intervening air are minimized.

Prototype perforated semiconductor neutron detectors addressing both the personal dosimetry and position sensitivity needs have been developed (McGregor et al., 2009; Jahan et al., 2007; Dunn et al., 2007). Individual detectors can be packaged in small, rugged, battery-powered containers to be worn as active dosimeters that can be read in real time. Similarly, arrays of perforated detectors can be assembled and used as high-resolution position-sensitive neutron detector arrays. The characterization of prototype detectors developed for both purposes is considered herein. The new detectors consist of silicon semiconductor material perforated using plasma-etching techniques. The perforations are filled and the top surface is coated with neutron-reactive ^6LiF . Neutrons interact in the reactive material and produce detectable

* Corresponding author. Tel.: +1 785 532 5628; fax: +785 532 7057.
E-mail address: dunn@mne.ksu.edu (W.L. Dunn).

reaction products from the ${}^6\text{LiF}(n,t){}^4\text{He}$ reaction. Combining the filled cavities with the traditional surface coatings leads to significant improvement in detector efficiency.

2. Neutron dosimeter

A prototype neutron dosimeter was constructed and tested. Because dosimeters worn on the body are affected by radiation backscattered from the body, an anthropomorphic torso phantom was used to characterize the dosimeter. Thermoluminescent dosimeters were used to estimate neutron dose at the surface of the phantom when irradiated by a neutron beam from the tangential beam tube of the TRIGA Mark II reactor at Kansas State University (KSU). Then, a prototype dosimeter was tested, with and without a cadmium backing. The prototype dosimeter provides LED readout of total counts, which then were related to dose. Use of both bare and cadmium-backed detectors within the dosimeter package can provide some information about the neutron spectrum. Future dosimeters will provide LED readout directly in dose units.

The detector incorporated in the prototype dosimeter was a cylindrical silicon diode having an active diameter of 6 mm, which was etched with 9681 cylindrical holes. Each hole was 30 μm in diameter and 76.6 μm deep. The holes were filled with ${}^6\text{LiF}$ and the top of the detector was coated with a layer of ${}^6\text{LiF}$ of thickness 39.5 μm . This design significantly increases the probability that an ejected reaction product will reach the semiconductor substrate and thus be detected.

The prototype dosimeter tested contained only a single bare detector, 3 AAA cell batteries, micro-electronics, and an LED readout in a package about 6 cm \times 5 cm \times 3 cm (see Fig. 1). Future devices will contain both bare and cadmium-backed detectors.



Fig. 1. Photograph of the first-generation neutron dosimeter package. The LED displays the total number of counts recorded since the device was last reset; the display is reset by pushing the reset button visible below the digital display.

2.1. Experimental procedure

A Biodex Medical¹ anthropomorphic torso phantom was used for characterization of the neutron dosimeter. The phantom consists of a body-shaped cylinder with lung, liver, and spine inserts. Lung inserts are filled with Styrofoam beads and the phantom is filled with water in order to simulate appropriate local densities. Nevertheless, the composition of the phantom is somewhat different from that of the human body in that there is no nitrogen in the phantom. Also, the phantom has no ribs. Nevertheless, our phantom, which we call “Harry,” simulates much of the anatomical structure of the upper torsos of an average male or female.

Thermoluminescent dosimeters (TLDs) were used to estimate the neutron dose on the surface of Harry due to a mixed-field beam from the TRIGA reactor. The gamma-ray portion of this dose must be separated from the total dose in order to estimate the neutron portion. The TLD-600 dosimeters contained 95.6% ${}^6\text{Li}$ whereas the TLD-700 dosimeters contained 0.007% ${}^6\text{Li}$ and so the TLD-700 dosimeters are thus unresponsive to neutrons. Therefore in a mixed n - γ field, the TLD-600 response is given by

$$R_{600}^{\gamma+n} = R_{600}^{\gamma} + R_{600}^n, \quad (1)$$

while the TLD-700 response is simply

$$R_{700}^{\gamma+n} = R_{700}^{\gamma} \quad (2)$$

with k defined as

$$k = \frac{R_{600}^{\gamma}}{R_{700}^{\gamma}}, \quad (3)$$

the neutron response in a mixed field can be obtained from

$$R_{600}^n = R_{600}^{n+\gamma} - kR_{700}^{\gamma}, \quad (4)$$

if the value of k is known.

To estimate the value of k , both TLD-600 and TLD-700 dosimeters were irradiated using a Panoramic Irradiator, which contained a ${}^{137}\text{Cs}$ source with known source strength. The initial charge (before irradiation) of each TLD was recorded. TLDs were placed at five positions (20, 30, 40, 50, and 60 cm from the source) and were irradiated for 40 min. The initial charge of each TLD was subtracted from the final charge. The dose rate at each position could be estimated by

$$D = \frac{S_0}{4\pi r^2} \mathfrak{R}, \quad (5)$$

where S_0 is the source strength (s^{-1}), r the source-to-dosimeter distance in cm, and \mathfrak{R} the response function in Svcm^2 . The average value of k determined from the readings at the five different distances was $k=0.849 \pm 0.030$.

2.2. Neutron dose on the surface of the phantom

An experiment was performed using the tangential beam port of the TRIGA Mark II reactor at Kansas State University (KSU). A shutter was used to open and close the beam and a beam catcher was placed behind the phantom. A TLD pair (TLD-600 and TLD-700) was placed in the middle of the front of the phantom, Harry, which was positioned 1 m from the shutter. The TLD pair was irradiated at a reactor power of 100 kW for 1.5 h. The same experimental procedure was repeated with a cadmium sheet between the TLD pair and Harry. The TLD responses were read out using a Harshaw 2000-C model reader at a heating ramp rate of 10 C s^{-1} from 135 to 265 C in a nitrogen atmosphere.

¹ Biodex Medical Systems, Inc., 20 Ramsay Road, Shirley, NY 11967.

The initial charge for each TLD was recorded and subtracted from the final charge after irradiation. The bare and Cd-filtered responses due to neutrons were calculated, using Eq. (4) and the experimentally determined value of k . The bare TLD-600 neutron dose rate per kW of reactor power was determined to be

$$D_n^b = 15.428 \pm 0.309 \text{ mSv h}^{-1} \text{ kW}^{-1} \quad (6a)$$

and the cadmium-filtered dose rate per kW was determined to be

$$D_n^f = 13.909 \pm 0.286 \text{ mSv h}^{-1} \text{ kW}^{-1}. \quad (6b)$$

The uncertainties were estimated assuming 2% uncertainty in the TLD responses and the specified uncertainty in the value of k .

2.3. Neutron dosimeter responses

The neutron dosimeter counts were observed after placing the dosimeter on Harry with the display facing the beam (see Fig. 2). The dosimeter was irradiated at a reactor power of 1 kW for times of 5, 10, and 15 min. The same experimental procedure was repeated after filtering the dosimeter with a cadmium sheet between the dosimeter and Harry. Dosimeter counts N were recorded for each configuration. The count-to-dose conversion factors $C = D_n/N$ and their standard deviations were determined and are given in Table 1. The inverses of these quantities indicate that the dosimeter records of order 10 counts/ μSv^{-1} . These experimental results compare favorably with simulation results (using the MCNP5 code), which indicate (see Jahan et al., 2007)



Fig. 2. The torso phantom, Harry, shown with the dosimeter mounted on the chest. The neutron beam from the reactor tangential beam tube enters from the left. The oscilloscope probes shown are not required for normal operation of the dosimeter.

that a boron-loaded Si detector whose efficiency is about 15% also will record of order 10 counts/ μSv^{-1} .

Count-to-dose conversion factors determined as above can be used, in principle, to convert dosimeter readout in counts into dose units. However, the actual dose will depend on the energy spectrum of the neutrons. Thus, we define a spectrum factor as

$$S = \frac{N_b - N_c}{N_b}, \quad (7)$$

where N_b is the total count of the bare detector and N_c the total count of the cadmium-filtered detector. Simulations show, for instance, that S is larger for a ^{235}U reactor Watt spectrum (~ 0.43) than for a room-temperature Maxwellian spectrum (~ 0.23).

3. Linear-array neutron detector

Two 32-channel prototype linear-array modules, whose channels were $120 \mu\text{m}$ wide \times 4 cm long, were constructed and characterized. Based on these prototypes, 64-channel modules will be constructed and combined to form a 1024-channel linear array for use at the Spallation Neutron Source (SNS) at Oak Ridge, TN. The p-type silicon region is the active part of each detector channel and is bounded by an n-type border on each side, as shown in Fig. 3.

The first prototype was a 32-channel device, like that depicted in Fig. 3, in which each $100 \mu\text{m}$ wide p-type region had an aluminum “trace” deposited, as shown in Fig. 4, to improve charge collection. The entire top surface then was coated with $10 \mu\text{m}$ of ^6LiF . In the second prototype, a $30 \mu\text{m}$ wide trench, $100 \mu\text{m}$ deep, was plasma etched into each channel. Each channel also had an aluminum trace deposited. The trenches were filled and the top surface was covered with ^6LiF ($26 \mu\text{m}$ cover thickness). In both prototypes, alternate channels were connected to bonding pads on each end of the detector, as depicted in both Figs. 4 and 5.

Preamplifier/shaper integrated circuits called Patara chips, were designed by colleagues at the University of Tennessee. Each Patara chip contains 32,000 transistors and allows readout of 16 channels. Thus two Patara 1 chips are needed for each 32-channel module called a high efficiency neutron detector array or HENDA. Each of the two HENDAs was wire-bonded to a daughter card, which connected the HENDA to the two Patara chips and transmitted 1.4V reverse bias voltage to the detector module. A schematic layout of the HENDA system is given in Fig. 6.

The detector motherboard was developed by the Electronics Design Laboratory (EDL) at KSU. A power supply was connected to the motherboard, which supplied power to various components ($+4.00\text{v}$ for digital communication, $+6.00\text{v}$ for each Patara chip, and -6v for the lower level discriminator (LLD) reference). The motherboard also transmitted neutron data to an optical communication card (OCC), as shown in Fig. 6. The OCC, developed by ORNL, contained a data server called “Dcomserver” and

Table 1
Counts from the dosimeter mounted on Harry for three different irradiation times with the reactor operating at 1 kW, equivalent doses, and the dose-count conversion factors.

Irrad. time (min)	N (counts)	D_n (μSv)	$\sigma(D_n)$ (μSv)	$C = D_n/N$ ($\mu\text{Sv count}^{-1}$)	$\sigma(C)$ ($\mu\text{Sv count}^{-1}$)
Bare					
5	12,533	1285.68	25.78	0.1026	0.0023
10	25,114	2571.37	51.55	0.1024	0.0022
15	37,484	3857.05	77.33	0.1029	0.0021
Cadmium-filtered					
5	11,968	1159.09	23.79	0.0968	0.0022
10	23,886	2318.19	47.59	0.0971	0.0021
15	36,153	3477.28	71.38	0.0962	0.0020

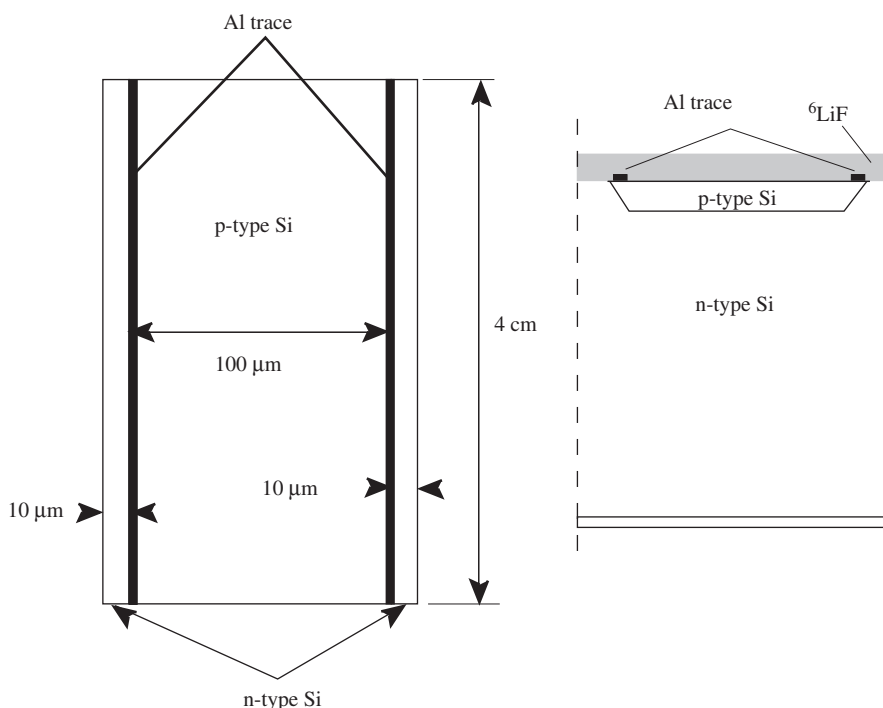


Fig. 3. Top (left) and side (right) views of a single linear-array channel of the planar device (not to scale). The top view shows the channel before the ${}^6\text{LiF}$ cap layer is added, the side view after. The 100- μm -wide p-type silicon creates a p–n junction with the bulk n-type silicon. In each trenched device, a 30 μm wide trench penetrates through the p-type layer and into the n-type bulk region and is filled with ${}^6\text{LiF}$.

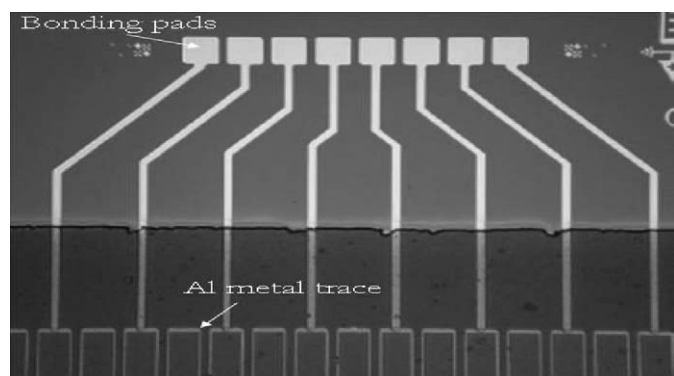


Fig. 4. A portion of one end of the planar device, showing bonding pads for eight of the 32 channels. Two sets of such bonding pads are used for the even-numbered channels and another two sets are used at the other end of the device for the odd-numbered channels.

transmitted commands from Dcomserver to the detector motherboard and received raw neutron data from the detector motherboard. The Dcomserver, developed by ORNL and modified by EDL, served as the user interface for HENDA. It was used to set odd and even global LLD settings, to control acquisition time, to display data (as histograms) in both one-sec snapshot and cumulative forms and to save data in text files.

3.1. HENDA pulse characterization and dead time

Pulses from a single channel of each HENDA were recorded, from which pulse characteristics such as pulse height, rise time, pulse duration, and signal-to-noise ratio could be estimated. The magnitudes of the pulses from all the HENDAs were similar measuring 550 ± 30 mV. Other characteristics of the pulses are summarized in Table 2.

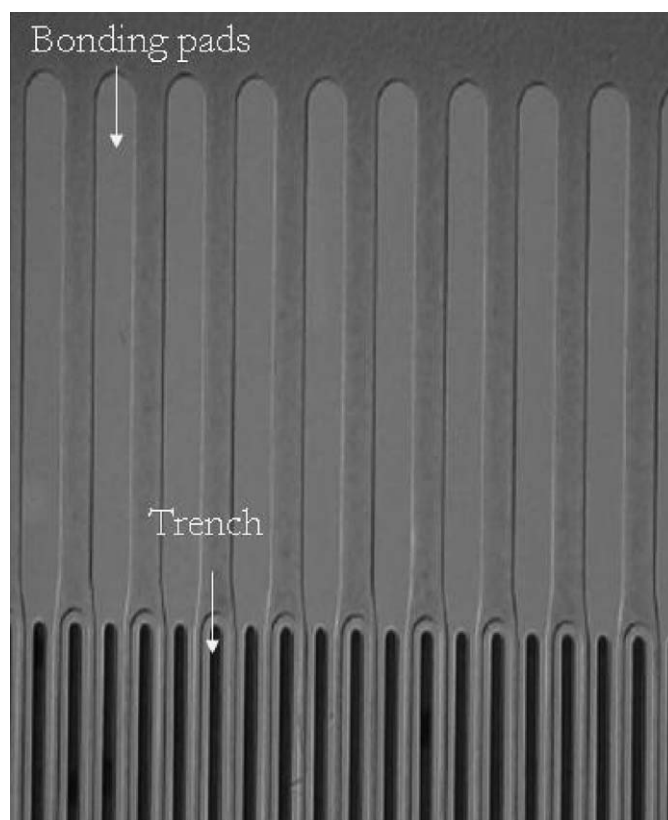


Fig. 5. A portion of one end of the trenched device, showing a different type of bonding pad and the trenches perforated into the silicon substrate.

A dead-time experiment was conducted at the tangential beam port of the KSU reactor as power levels were doubled from 2 to 512 kW. A count time of 75 s was used for both the planar and

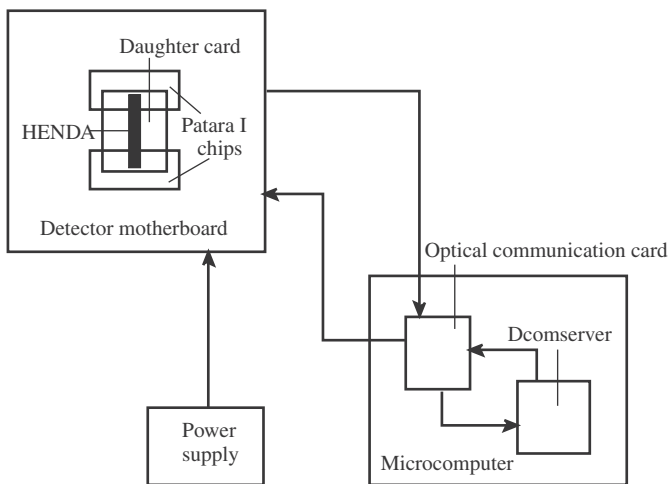


Fig. 6. The schematic layout of the HENDA system is shown, with the subcomponents of the three major components identified.

Table 2

The measured pulse characteristics of the three HENDAs tested.

HENDA	Rise time (μs)	Total duration (μs)	Signal-to-noise ratio
Planar	0.32	1.24	42:1
100 μm trenched	0.20	1.00	42:1
175 μm trenched	0.30	1.80	40:1

100- μm -deep trenched devices. The neutron responses for both HENDAs tested was linear from 2 to 512 kW. Knowing the thermal neutron flux from the tangential beam port, we conclude that the HENDAs experience negligible dead time for neutron intensities up to at least $10^6 \text{ cm}^{-2} \text{ s}^{-1}$.

3.2. HENDA spatial resolution

The spatial resolution of the HENDA prototypes should be 120 μm , to within the construction precision, which is presumed to be very good. However, one can treat the HENDA as a detector with unknown resolution and conduct a knife-edge test to measure the resolution. We used a Gd knife-edge layer on Si backing, producing a very good neutron filter along one dimension. The knife edge was placed in front of each HENDA and then each HENDA was translated 250 μm horizontally through a neutron beam in 25 μm increments. The response of the planar device at one position relative to the knife edge is shown in Fig. 7.

The spatial resolution for the planar detector array was confirmed by measuring the full-width at half-maximum (FWHM) of the line-spread function (LSF), which is the first derivative of the edge-spread function (ESF) (Uher et al., 2005). Counts obtained as the HENDA was moved relative to the knife edge were used to produce a plot to which the ESF, given by

$$e(x) = a \operatorname{erf}[b(x - c)] + d \quad (8)$$

were fit, where $\operatorname{erf}(x)$ is the error function, x is the relative distance that HENDA traveled from the knife-edge, and a , b , c , and d are constants used to best fit Eq. (8) to the data. The parameter d obviously is related to the neutron background. The LSF is given by the first derivative of the ESF (Uher et al., 2005), i.e.,

$$\ell(x) = \frac{de(x)}{dx} = \frac{2ab}{\sqrt{\pi}} \exp[-b^2(x - c)^2]. \quad (9)$$

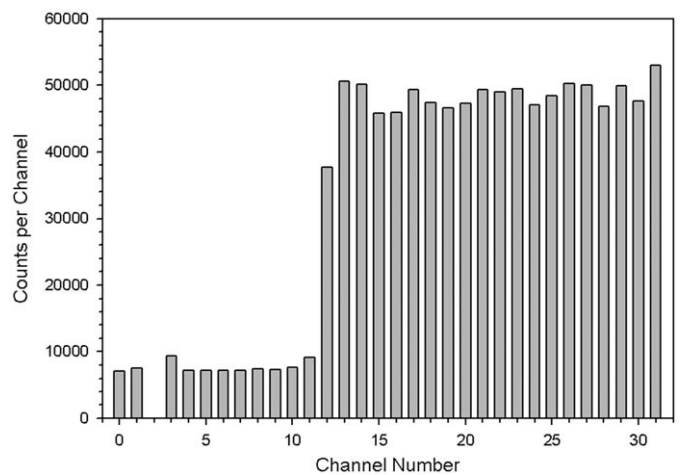


Fig. 7. The output from each channel with the Gd knife edge positioned partially over channel 12. Note that channel two is not counting appreciably.

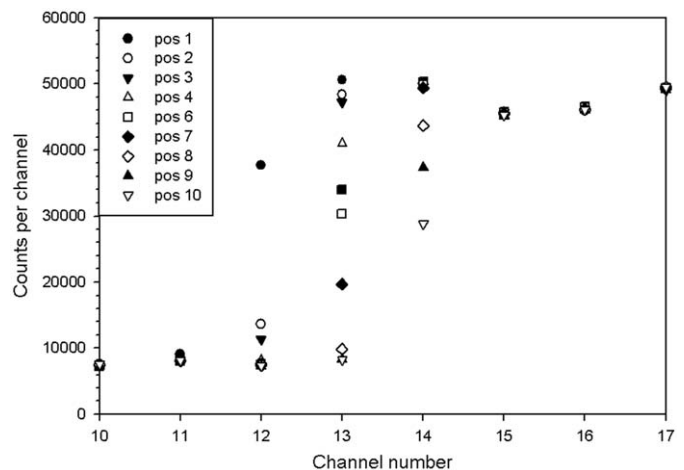


Fig. 8. A plot of total counts per channel, for channels 10–18 of the planar device, versus channel number for ten positions of the knife edge relative to the HENDA. The HENDA was moved 25 μm relative to the fixed knife edge between successive data collections.

Eq. (9) is just a Gaussian shape with a variance given by

$$\sigma^2 = \frac{1}{2b^2}. \quad (10)$$

The full-width at half-maximum (FWHM) of a Gaussian is $\text{FWHM} = 2\sqrt{2\ln(2)}\sigma$ and the resolution of the detector is given by the FWHM. Thus, we find that

$$\text{Resolution} = \frac{2\sqrt{\ln(2)}}{b}. \quad (11)$$

The data collected from channels 10 through 18 are displayed in Fig. 8, in which Pos 1 refers to the data collected with the HENDA at the original position behind the knife edge, Pos 2 refers to the data collected after the HENDA was moved leftward 25 μm and so forth. It is apparent that the knife edge was initially partially covering channel 12 and ended partially covering channel 14. Thus, the counts in channel 13 can be used to obtain the edge- and line-spread functions. Eq. (8) was fit to the Edge Spread Function data by MathCad; the values of the best-fit parameters were $a=22,300$, $b=0.01358 \mu\text{m}$, $c=122.8 \mu\text{m}$, and $d=27,950$. The data and the fit are shown in Fig. 9 and the Line Spread Function is shown in Fig. 10. From Eq. (10), a spatial

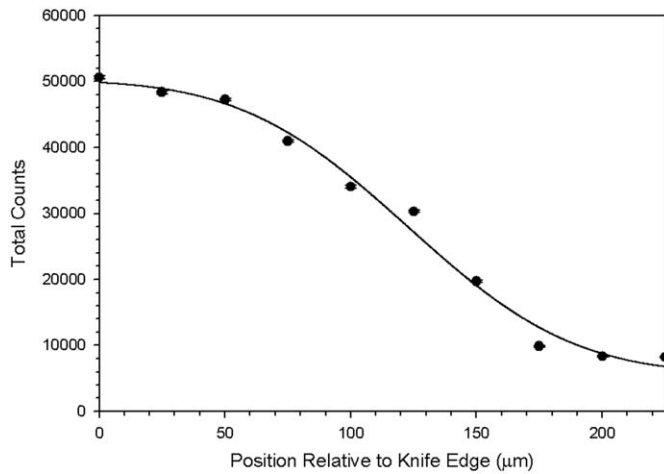


Fig. 9. The edge-spread data and functional fit for channel 13 of the planar device.

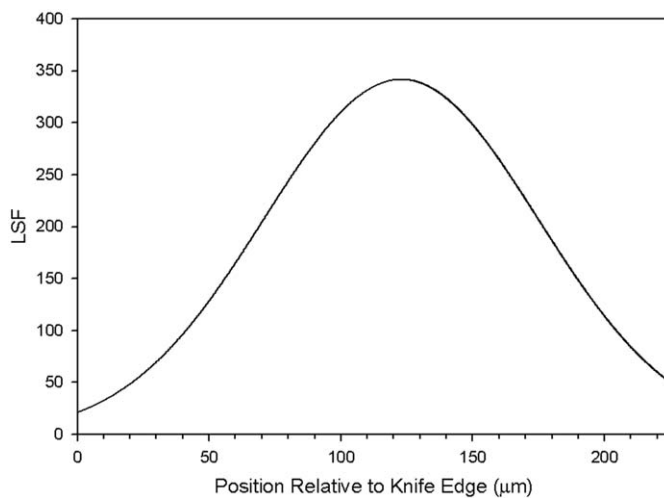


Fig. 10. The Gaussian line-spread function for channel 13 of the planar device. The resolution of the detector was estimated from the FWHM of this Gaussian.

resolution of 122.6 μm was obtained, which confirms the resolution to within 2%.

3.3. Thermal neutron detection efficiency

The HENDA neutron counting efficiency was determined using a monoenergetic neutron flux from the diffracted neutron beam at the northwest beam port of the KSU TRIGA Mark II reactor. A silicon crystal was used to create a monoenergetic beam at approximately 0.0253 eV, the most probable neutron energy of a thermal neutron at room temperature. A collimator was made by drilling a 1.5 mm diameter hole in a 2.54 cm × 2.54 cm × 2.54 cm BC₄ block. The HENDA was aligned with the collimation hole by translating the array until 13 channels (the maximum number of channels that could be exposed to the collimated beam) were counting. Shutter-open and shutter-closed responses were recorded for both HENDAs and for a ³He detector with the reactor operating at 200 kW, so that net count rates could be determined.

A ³He detector with known efficiency was used and the HENDA efficiencies were measured relative to this. Thus, the HENDA efficiency is given by

$$\varepsilon_x = \frac{m_x}{m_{\text{He-3}}} \varepsilon_{\text{He-3}}, \quad (12)$$

where ε_x is the efficiency of detector x (with x standing for planar or trenched), m_x is the net count rate obtained with HENDA x , and $m_{\text{He-3}}$ is the net count rate of the ³He detector. These net count rates were determined as follows:

$$m = \frac{C_o}{T_o} - \frac{C_c}{T_c}, \quad (13a)$$

where C_o and T_o are the total counts and counting time with the shutter open, respectively, and C_c and T_c are the total counts and counting time with the shutter closed, respectively, for each HENDA and

$$m_H = \frac{C_{Ho}}{T_{Ho}} - \frac{C_{Hc}}{T_{Hc}}, \quad (13b)$$

where C_{Ho} and T_{Ho} are the total counts and counting time with the shutter open, respectively, and C_{Hc} and T_{Hc} are the total counts and counting time with the shutter closed, respectively, for the ³He detector. The ³He detector efficiency at 0.0253 eV is $\varepsilon_{\text{He-3}} = 83.5\%$.

The neutron counting efficiencies for the planar and 100 μm trenched devices were determined by Eq. (12) to be 1.2% and 12.5%, respectively, both good to within a few percent of the values given. This is consistent with other experiments that were conducted to characterize the HENDA prototypes in which the neutron-counting efficiency of the trenched device was seen to be approximately 10 times the neutron-counting efficiency of the planar device.

3.4. Future developments

The thermal-neutron detection efficiency of the single-layer trenched prototype device tested can be essentially doubled by employing a 'sandwich' design in which two single-layer devices are sandwiched together with the perforations in one offset from the perforations in the other. Also, a 1024-channel detector is being constructed for delivery to the Spallation Neutron source that will be constructed of sixteen 64-channel devices, each 4 cm long and having 100 μm pitch. The resulting linear array detector will be approximately 10.24 cm wide by 4 cm tall and, employing the sandwich design, will operate with a thermal neutron detection efficiency of 25% or more.

5. Discussion and conclusions

Portable, real-time, gamma-insensitive neutron dosimeters can be produced using perforated neutron semiconductor detectors. The prototype dosimeter tested produced about 10 counts μSv⁻¹. Thus, it is possible to convert the dosimeter counts into dose units. Using both bare and cadmium-backed detector responses, one can gain a general idea of the type of neutron spectrum. The dosimeters account for neutron scattering in the torso of a phantom or the body. These dosimeters are compact and light enough to be worn on the body, are insensitive to gamma radiation, are able to operate continuously, and provide real-time output in counts or dose units.

A 32-channel linear array prototype module was constructed and tested. The detection efficiency of single-layer devices is about an order of magnitude greater than that for coated semiconductor devices. These efficiencies can be increased by employing a sandwich design with two layers whose perforations are offset from one another. The prototype device was able to operate with negligible dead time in thermal neutron fields of up to at least 10⁶ cm⁻² s⁻¹. The technology is being extended to construct 64-channel devices, which can then be combined to form a linear array neutron detector with about 1000 channels in a 10 cm wide by 4 cm long linear array detector system.

Acknowledgments

The authors acknowledge financial support from the US Department of Energy (DOE). Also thanks are due to Dr. Phil Ugorowski and Mr. Edgar Martinez for their assistance with the experimental testing.

References

- Aschan, C., Toivonen, M., Savolainen, S., Seppälä, T., Auterinen, I., 1999. Epithermal neutron beam dosimetry with TL dosimeters for boron neutron capture therapy. *Radiat. Prot. Dosim.* 81, 47–56.
- Badhwar, G.D., 2002. Shuttle radiation dose measurements in the International Space Station orbits. *Radiat. Res.* 157, 69–75.
- Dunn, W.L., Jahan, Q.M., McGregor, D.S., McNeil, W.J., Patterson, E.L., Rice, B.B., Shultis, J.K., Soloman, C.J., 2007. Design and performance of a portable neutron dosimeter. In: *Proceedings of the Second Workshop on European Collaboration for Higher Education and Research in Nuclear Engineering and Radiological Protection*, 13–15 March 2006, Valencia, Spain, pp. 85–92.
- Esposito, A., Nandy, M., 2004. Measurement and unfolding of neutron spectra using Bonner spheres. *Radiat. Prot. Dosim.* 110 (1–4), 555–558.
- ICRU, 2001. Determination of operational dose equivalent quantities for neutrons. Report 66, International Commission on Radiation Units and Measurements, Bethesda, MD.
- Ing, H., Piesch, E., 1985. Status of neutron dosimetry. *Radiat. Prot. Dosim.* 10 (1–4), 5–15.
- Jahan, Q., Patterson, E., Rice, R., Dunn, W.L., McGregor, D.S., 2007. Neutron dosimeters employing high-efficiency perforated semiconductors. *Nucl. Instrum. Methods Phys. Res. B* 263 (1), 183–185.
- Knoll, G.F., 2000. *Radiation Detection and Measurement*, third ed. John Wiley & Sons, New York, NY.
- McGregor, D.S., Hamming, M.D., Gersch, H.K., Yang, Y.-H., Klann, R.T., 2003. Design considerations for thin film coated semiconductor thermal neutron detectors, part I; basics regarding alpha particle emitting neutron reactive films. *Nucl. Instrum. Methods Phys. Res. A* 500, 272–308.
- McGregor, D., Bellinger, S.L., Bruno, D., Dunn, W.L., McNeil, W.J., Patterson, E., Rice, B.B., Shultis, J.K., Unruh, T., 2009. Perforated diode neutron detector modules fabricated from high-purity silicon. *Radiat. Phys. Chem.*, 78, 874–881.
- Nicholson, K.P., Snelling, G.F., 1955. Some lithium iodide phosphors for slow neutron detection. *Br. J. Appl. Phys.* 6, 104–106.
- Piesch, E., Burgkhardt, B., 1985. Albedo neutron dosimetry. *Radiat. Prot. Dosim.* 10, 175–188.
- Riel, G., Rao, N., Kerschner, H., Nelson, M., 1991. Superheated drop, “bubble”, neutron dosimeter performance in a work environment. *IEEE Trans. Nucl. Sci.* 38 (2), 494–496.
- Uher, J., Holy, T., Jakubek, J., Lehmann, E., Pospisil, S., Vacik, J., 2005. Performance of a pixel detector suited for slow neutrons. *Nucl. Instrum. Methods Phys. Res. A* 542, 283–287.